# The use of ALOS data in studying environmental changes in Malaysia

**PI No. 404**
**Dr. Lim Hwee San**[(1)]
**Assoc. Prof. Dr. Mohd. Zubir Mat Jafri**[(2)], **Assoc. Prof. Dr. Khiruddin Abdullah**[(3)], **Assoc. Prof. Nasirun Mohd. Saleh**[(4)],
**Dr. Norhaslinda Mohamed Tahrin**[(5)]

[(1)] Lecturer, School of Physics, Universiti Sains Malaysia, 11800 Penang, Malaysia, E-mail: hslim@usm.my
[(2)] Lecturer, School of Physics, Universiti Sains Malaysia, 11800 Penang, Malaysia, E-mail: mjafri@usm.my
[(3)] Lecturer, School of Physics, Universiti Sains Malaysia, 11800 Penang, Malaysia, E-mail: khirudd@usm.my
[(4)] Lecturer, School of Physics, Universiti Sains Malaysia, 11800 Penang, Malaysia, E-mail: nasirun@usm.my
[(5)] Lecturer, School of Physics, Universiti Sains Malaysia, 11800 Penang, Malaysia, E-mail: haslinda@usm.my

### Summary of originally proposed research

Remote sensing data have been widely used in environmental studies like land cover change, flood observation, environmental pollution monitoring. This study is dealing with obtaining land cover, flood observation and environmental pollution using ALOS data. With the availability of remotely sensed and in situ data sets the derivable geophysical parameters are water depth, sea surface temperature (SST) and sediment (suspended matter) concentration. Understanding of the optical properties of water and the atmospheric contribution serves as a basic for the derivation of algorithms for specific applications using data in the visible and the near infrared regions. For the thermal region atmospheric absorption and the surface thermal properties are considered for the development of the SST algorithm. Analyses of time series of remote sensing images with regard to the variation of the water quality parameters of interest are required. In situ water samples coincident with the remote sensing data will be collected. Measurements of the in situ water quality parameters are performed at selected locations within the studied area, i.e. water areas surrounding Penang Island. Surface and vertical profile of sediment concentrations will be measured. This will be done at various locations along the coastal and during diurnal various times of the year. The time scheme for the data collection will be covering different seasons of the year. Satellite scenes that coincide simultaneously with the in situ data will be employed.

Several processing steps will be performed to the remote sensing data for water quality maps generation:

1. Geometric correction - images will be rectified to the corresponding maps or coordinate system of the area.
2. Atmospheric correction – the darkest pixel method will be applied to reduce atmospheric contamination on the scenes. Other methods will also be investigated. Cloud masking will be performed to the thermal data.
3. Algorithm calibration, regression analysis – regression analysis will be performed to determine the optimum algorithm for each application.
4. Generation of water quality maps – the calibrated algorithm will be applied to the remote sensing data sets for establishing water quality maps.
5. Interpretation and modeling – from the retrieved information, detailed interpretation can be made.

Human-induced changes in land cover are as ancient as humankind itself. Society's demand for physical resources, and the expansion of its technological, managerial, and institutional capacity to produce, move, and consume such resources, have long altered land vegetation and other surface features. The characteristics of land cover have important impacts on climate, global biogeochemistry, and the abundance and composition of terrestrial species. The land cover will be mainly derived from visual interpretation of recent high resolution satellite images digitally enhanced. In this study, we propose to use high resolution satellite imagery to map areas of forest clearing and general land cover types for the entire Peninsular Malaysia region. In this study, the supervised and unsupervised classifications techniques will be used to generate thematic land cover maps. And then their accuracy will be determined by the Kappa Coefficient and overall accuracy. The thematic interpretation of ALOS data and the validation of the land cover map will be supported by available Landsat TM images, SPOT images and IRS data, and vegetation maps and field data collected in the region. The resulting land cover map will be integrated in a socio-economic study to assess the trends and patterns of deforestation by including demographic and social and environmental policies. Finally, we also will study the land cover changes over the study areas. There were two steps involved in identifying land cover changes using the

ALOS imagery: 1) identify the land cover types on both of the ALOS images, and 2) compare the land cover types on the ALOS images to determine which areas represented land cover changes. In this study, we also will investigate the coincident distribution, and detailed patterns in space and time of land cover, land-cover attributes, and land-cover change. Several processing steps will be performed to the remote sensing data:

1. Geometric correction - images will be rectified to the corresponding maps or coordinate system of the area.
2. Atmospheric correction – the darkest pixel method will be applied to reduce atmospheric contamination on the scenes. Other methods will also be investigated. Cloud masking will be performed to the thermal data.
3. Classification analysis – two classification techniques analysis will be performed to determine the land cover types.
4. Accuracy assessments – Kappa Coefficient will be performed to determine the accuracy of the classified maps.
5. Generation of land covers maps – the best produced accuracy classifier will be used to generate land cover maps.
6. Land cover changes interpretation – from the generated land cover maps, detailed land cover changes can be made.
7. Interpretation and modeling – from the retrieved information, detailed interpretation can be made.

*Keywords:* Water Quality, TSS, Land Cover.

## 1. INTRODUCTION

Although accurate measurements of water and air quality parameters can be obtained with a conventional measuring technique, such a survey is time consuming and expensive. Consequently, investigators have become interested in the application of remotely sensed data to overcome these limitations. Remote sensing is an effective technique for air and water quality mapping through the analysis of digital images. Satellite data have been successfully employed to map coastal and inland water areas.

Land cover analysis plays an important role in many environmental applications nowadays. Satellite images can provide a high spatial resolution land cover map. This study investigated the potential of using digital camera for land cover mapping over Kedah, Malaysia using ALOS AVNIR data. The standard supervised classification techniques, such as the maximum likelihood, minimum distance-to-mean, parallelepiped, neural network and frequency based contextual classifier were applied to the multispectral satellite images.

**- Research objectives:**

- To determining environmental changes over Malaysia.

- To finding the features of the land cover.
- To develop algorithms and techniques for measuring water and air pollution level from ALOS satellite images by using the remote sensing technique.

**- Research implementation:**

Basically, we archived the research objectives and target that we set before throughout the research in the phase 1 (by the time of this interim report). Everything was following the original research plan. We were successfully mapping the environmental pollution level. In this project, we also successfully map the particulates matter of less than 10-micro in diameter (PM10) using ALOS data.

## 2. STUDY AREA AND DATA ACQUISITION

### 2.1 Study Area

The study area is the Penang Island and Yan, Kedah, Malaysia, located within latitudes $5^o$ 12' N to $5^o$ 30' N and longitudes $100^o$ 09' E to $100^o$ 26' E. The map of the region is shown in Figure 1.



**Fig 1. Study area**

### 2.2 Data Acquisition

The satellite image was acquired on 24 April 2007 captured by satellite ALOS – AVNIR-2. The satellite data was in 1B2 product level.
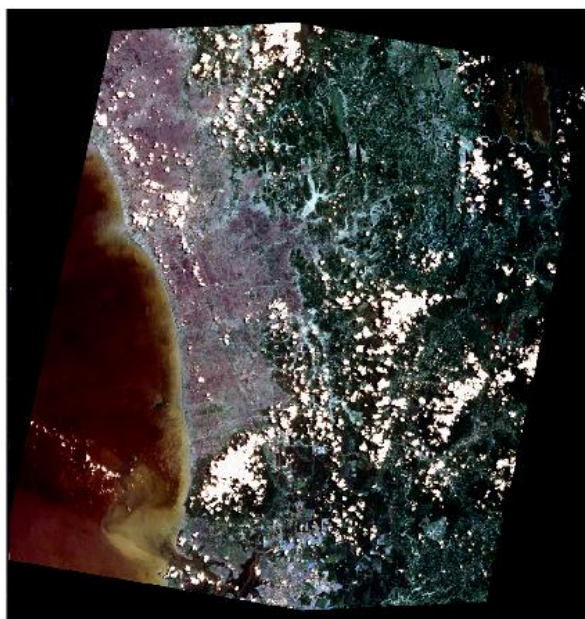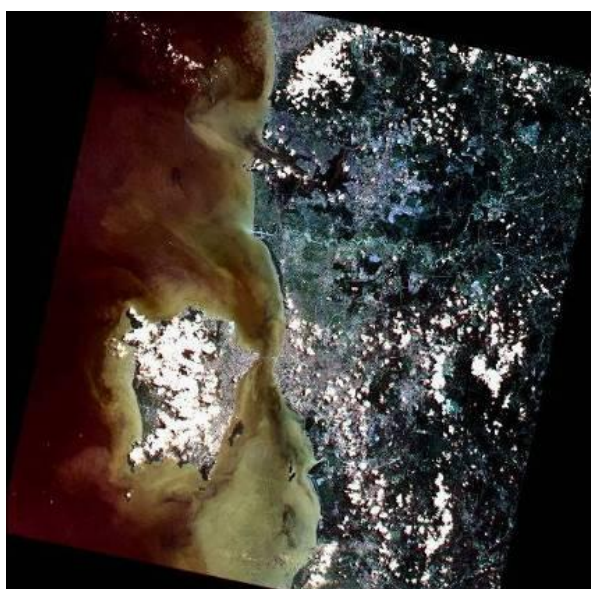
**Fig. 2 Raw satellite image used in this study**



**Fig. 3 Raw satellite image used in this study**

The Japanese Earth observing satellite program consists of two series: those satellites used mainly for atmospheric and marine observation, and those used mainly for land observation. The Advanced Land Observing Satellite (ALOS) follows the Japanese Earth Resources Satellite-1 (JERS-1) and Advanced Earth Observing Satellite (ADEOS) and will utilize advanced land-observing technology. ALOS will be used for cartography, regional observation, disaster monitoring, and resource surveying.
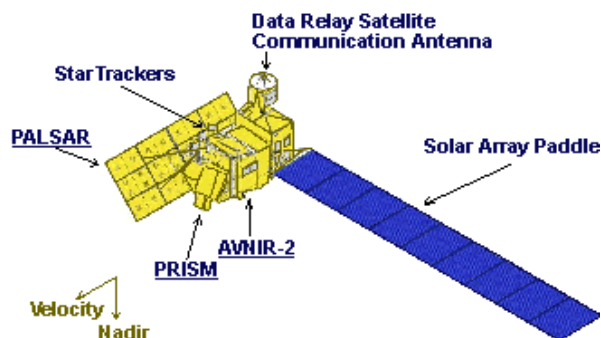


**Fig. 4 ALOS Satellite**

The ALOS has three remote-sensing instruments: the Panchromatic Remote-sensing Instrument for Stereo Mapping (PRISM) for digital elevation mapping, the Advanced Visible and Near Infrared Radiometer type 2 (AVNIR-2) for precise land coverage observation, and the Phased Array type L-band Synthetic Aperture Radar (PALSAR) for day-and-night and all-weather land observation. In order to utilize fully the data obtained by these sensors, the ALOS was designed with two advanced technologies: the former is the high speed and large capacity mission data handling technology and the latter is the precision spacecraft position and attitude determination capability. They will be essential to high-resolution remote sensing satellites in the next decade. ALOS have been successfully launched on an H-IIA launch vehicle from the Tanegashima Space Center, Japan.

The Advanced Land Observing Satellite (ALOS) was launched on Jan 24th, 2006 onboard a JAXA H-IIA launcher. The planned operational lifetime is 3 years, in a near-polar, Sun-synchronous orbit, at a mean altitude of 691 km. Its payload consists of three sensors: Advanced Visible and Near Infrared Radiometer type 2 (AVNIR-2), Panchromatic Remote sensing Instrument for Stereo Mapping (PRISM), Phased Array type L-band Synthetic Aperture Radar (PALSAR). The coverage and distribution of ALOS data is done through the implantation of the ALOS Data Node concept. The acquisitions performed globally are classified in four regions: Asia, Europe and Africa, America, Australia and Oceania.

## Table 1. ALOS Characteristics

| | |
|---|---|
| Launch Date | Jan. 24, 2006 |
| Launch Vehicle | H-IIA |
| Launch Site | Tanegashima Space Center |
| Spacecraft Mass | Approx. 4 tons |
| Generated Power | Approx. 7 kW (at End of Life) |
| Design Life | 3 -5 years |
| Orbit | Sun-Synchronous Sub-Recurrent |
| | Repeat Cycle: 46 days<br>Sub Cycle: 2 days |
| | Altitude: 691.65 km (at Equator) |
| | Inclination: 98.16 deg. |
| Attitude Determination Accuracy | $2.0 \times 10-4$degree (with GCP) |
| Position Determination Accuracy | 1m (off-line) |
| Data Rate | 240Mbps (via Data Relay Technology Satellite)<br>120Mbps (Direct Transmission) |
| Onboard Data Recorder | Solid-state data recorder (90Gbytes) |

Objectives

ALOS is one of the largest Earth observing satellites ever developed. Its objectives are:

- to provide maps for Japan and other countries including those in the Asian-Pacific region (Cartography)
- to perform regional observation for "sustainable development", harmonization between Earth environment and development (Regional Observation),

- to conduct disaster monitoring around the world (Disaster Monitoring),
- to survey natural resources (Resources Surveying),
- to develop technology necessary for future Earth observing satellite (Technology Development)

**AVNIR-2 -** Advanced Visible and Near Infrared Radiometer type 2

The Advanced Visible and Near Infrared Radiometer type 2 (AVNIR-2) is a visible and near infrared radiometer for observing land and coastal zones. It provides better spatial land-coverage maps and land-use classification maps for monitoring regional environments. AVNIR-2 is a successor to AVNIR that was on board the Advanced Earth Observing Satellite (ADEOS), which was launched in August 1996.

Its instantaneous field-of-view (IFOV) is the main improvement over AVNIR. AVNIR-2 also provides 10m spatial resolution images, an improvement over the 16m resolution of AVNIR in the multi-spectral region. Improved CCD detectors (AVNIR has 5,000 pixels per CCD; AVNIR-2 7,000 pixels per CCD) and electronics enable this higher resolution. A cross-track pointing functions for prompt observation of disaster areas is another improvement. The pointing angle of AVNIR-2 is +44 and - 44 degree.



**Fig. 5 AVNIR-2 Sensor**

**Table 2. AVNIR-2 Characteristics**

| | |
|---|---|
| Number of Bands | 4 |
| Wavelength | Band 1 : 0.42 to 0.50 micrometers<br>Band 2 : 0.52 to 0.60 micrometers<br>Band 3 : 0.61 to 0.69 micrometers<br>Band 4 : 0.76 to 0.89 micrometers |
| Spatial Resolution | 10m (at Nadir) |
| Swath Width | 70km (at Nadir) |

| S/N | >200 |
|---|---|
| MTF | Band 1 through 3 : >0.25<br>Band 4 : >0.20 |
| Number of Detectors | 7000/band |
| Pointing Angle | - 44 to + 44 degree |
| Bit Length | 8 bits |

Note: AVNIR-2 cannot observe the areas beyond 88.4 degree north latitude and 88.5 degree south latitude.

## 2.3 Algorithm Developed and Used In This Project

### 2.3.1 Water Quality-TSS

In this study, two algorithms will be developed and tested using the ALOS satellite data for water quality and air quality mapping. For the water quality algorithm, a physical model relating radiance from the water column to the concentrations of the water's constituents provides the most effective way to analyze remotely sensed data for water quality studies. Remote sensing reflectance, R, is related to the irradiance reflectance just beneath the water surface, Rird (Doxaran et al., 2002) and is calculated as:

$$R = \frac{(1-\rho)(1-\sigma)R_{ird}}{n^2(1-rR)Q}$$

(1)

where
$\rho$ = internal Fresnel reflectance
$\sigma$ = air-water Fresnel reflection at the interface
$r$ = water-air reflection
n = refractive index (1.34)
Q = $\pi$

Equation (1), according to Doxaran et al. (2002) can be approximated as

$$R = 0.182 \frac{R_{ird}}{Q}$$

(2)

For estuaries water, backscatter is much less significant than absorption (Gohin et al., 2002). Therefore, the irradiance reflectance just below the water surface (Morel and Prieur, 1977), Siddorn et al. (2001) and Kirk (1984)) is:

$$R_{ird} = 0.33 \frac{b}{a}$$

(3)

where
b = backscattering coefficient
a = absorption coefficient

Then equation (2) can be simplified to

$$R = c \frac{b}{Qa}$$

(4)

where c = a constant

The inherent optical properties are determined by the contents of the water. The contributions of the individual components to the overall properties are strictly additive (Gallegos and Correl, 1990). The total absorption coefficient at wavelength, $\lambda$, a($\lambda$), can be considered to be the sum of absorption due to pure water, aw($\lambda$), phytoplankton, ac($\lambda$), non-chlorophyllos particles of biological and terrestrial origin, ap($\lambda$), and dissolved organic matter or yellow substance, ay($\lambda$) [Gallegos and Correll, 1990]. Thus

$$a(\lambda) = a_w(\lambda) + a_c(\lambda) + a_p(\lambda) + a_y(\lambda)$$

(5)

The absorption of pure seawater is practically the same as the pure water in the visible region (400□700nm). Absorption by dissolved salts is known to be negligible in this region [Gallegos and Correll, 1990]. The absorption related to each substance is expressed as the product of its concentration C (phytoplankton), P (non-chlorophyllous particles), or Y (yellow substance) and its corresponding specific absorption coefficients ac*($\lambda$), ap*($\lambda$) and ay*($\lambda$) respectively.

Therefore the total absorption

$$a(\lambda) = a_w(\lambda) + a_c^*(\lambda)C + a_p^*(\lambda)P + a_y^*(\lambda)Y$$

(6)

Similarly for the back-scattering coefficients [Prieur and Sathyendranath, 1981]

$$b_b(\lambda) = b_{bw}(\lambda) + b_{bc}(\lambda) + b_{bp}(\lambda) + b_{by}(\lambda)$$

(7)

where bbw($\lambda$), bbc($\lambda$), bbp($\lambda$), and bby($\lambda$) are the back-scattering coefficients of water, chlorophyll, suspended matter and yellow substance respectively. Then

$$b_b(\lambda) = b_{bw}(\lambda) + b_{bc}^*(\lambda)C + b_{bp}^*(\lambda)P + b_{by}^*(\lambda)Y$$

(8)

The symbol * denotes specific coefficients. The magnitude of bbw($\lambda$) is 0.5bw($\lambda$) because the molecular volume-scattering function of pure sea water, bw($\lambda$), is symmetrical [(Gallie and Murtha, 1992)].

For a case involving three water quality components, e.g. chlorophyll, C, suspended sediment, P, and yellow substance, Y, the simultaneous equations using equations (4) to (8) for the three channels ($\lambda_1$, $\lambda_2$ and $\lambda_3$) can be expressed as:

$$R(\lambda_1) = R_2 = \frac{c}{Q} \frac{[0.5b_w(\lambda_1) + b_c^*(\lambda_1)C + b_p^*(\lambda_1)P + b_{by}^*(\lambda_1)Y]}{[a_w(\lambda_1) + a_c^*(\lambda_1)C + a_p^*(\lambda_1)P + a_y^*(\lambda_1)Y]} \quad (9)$$

$$R(\lambda_2) = R_2 = \frac{c}{Q} \frac{[0.5b_w(\lambda_2) + b_c^*(\lambda_2)C + b_p^*(\lambda_2)P + b_{by}^*(\lambda_2)Y]}{[a_w(\lambda_2) + a_c^*(\lambda_2)C + a_p^*(\lambda_2)P + a_y^*(\lambda_2)Y]} \quad (10)$$

$$R(\lambda_3) = R_3 = \frac{c}{Q} \frac{[0.5b_w(\lambda_3) + b_c^*(\lambda_3)C + b_p^*(\lambda_3)P + b_{by}^*(\lambda_3)Y]}{[a_w(\lambda_3) + a_c^*(\lambda_3)C + a_p^*(\lambda_3)P + a_y^*(\lambda_3)Y]} \quad (11)$$

where

$b_w(\lambda)$ = pure water backscattering coefficient

$b_c^*(\lambda)$ = chlorophyll specific backscattering coefficient

$b_p^*(\lambda)$ = sediment specific backscattering coefficient

$b_y^*(\lambda)$ = yellow substance specific backscattering coefficient

$a_w(\lambda)$ = pure water absorption coefficient

$a_c^*(\lambda)$ = chlorophyll specific absorption coefficient

$a_p^*(\lambda)$ = sediment specific absorption coefficient

$a_y^*(\lambda)$ = yellow substance specific absorption coefficient

$C$ = chlorophyll concentration

$P$ = suspended sediment concentration

TSS concentrations can be obtained by solving the simultaneous equations (9), (10) and (11) to yield the series consisting of the terms in $R_1$, $R_2$ and $R_3$ (ignoring higher order terms):

$$P = e_o + e_1 R_1 + e_2 R_2 + e_3 R_3 + e_4 R_1 R_2 + e_5 R_1 R_3 + e_6 R_2 R_3 + e_7 R_1{}^2 + e_8 R_2{}^2 + e_9 R_3{}^2 \quad (12)$$

where the coefficient $e_j$, $j = 0, 1, 2, \ldots$ are the functions related to the coefficients used in equations (9), (10) and (11) which are to be determined empirically from multiple regression analysis. This equation is used to relate reflectance values from the image bands to the observed TSS concentrations. In this study, we used digital number (DN) instead of $R$ values (see below).

## 2.3.2 Water Quality- Chlorophyll

A physical model relating radiance from the water column and the concentrations of the water quality constituents provide the most effective way of analysing remotely sensed data for water quality studies. Reflectance is particularly dependent on inherent optical properties: the absorption coefficient and the backscattering coefficient. The irradiance reflectance just below the water surface, R($\lambda$), is given [Kirk, 1984]

$$R(\lambda) = 0.33b(\lambda)/a(\lambda) \quad (13)$$
where
$\lambda$ = the spectral wavelength
b = the backscattering coefficient
a = the absorption coefficient

The inherent optical properties are determined by the contents of the water. The contributions of the individual components to the overall properties are strictly additive [Gallegos and Correl, 1990].

For a case involving water quality component, chlorophyll, C, the equation given by other studied [Gallie and Murtha, 1992] can be expressed as

$$R(\lambda_1) = R_1 = 0.33 \frac{(0.5b_{bw}(\lambda_1) + b_{bc}^*(\lambda_1)C)}{(a_w(\lambda_1) + a_c^*(\lambda_1)C)} \quad (14)$$

where

bbw($\lambda_i$) = backscattering coefficient

aw($\lambda_i$) = absorption coefficient
ap* = chlorophyll specific absorption coefficient
C = chlorophyll concentration

Chlorophyll concentration can be obtained by solving Equation (14) to Equation (15) that is given as

$$C = \frac{1 - \dfrac{a_w R(\lambda)}{0.165 b_{bw}}}{-\dfrac{0.33 b_{bC}^*}{0.165 b_{bw}} + \dfrac{a_C^*}{0.165 b_{bw}} R(\lambda)} \quad (15)$$

We have to know two parameters (the backscattering and absorption coefficients) to solve Equation 15. But these parameters were not available from this study area. So we used regression technique to solve the equation. From Equation 15, we can simplify the regression model as shown by Equation 16 for chlorophyll.

$$C = \frac{1 + a_0 R(\lambda)}{a_1 + a_2 R(\lambda)} \qquad (16)$$

where $a_0$, $a_1$ and $a_2$ was the algorithm coefficients that can be solved empirically.

### 2.3.3 Air Quality

For the water quality algorithm, the atmospheric reflectance due to molecule, $R_r$, is given by (Liu, et al., 1996)

$$R_r = \frac{\tau_r P_r(\Theta)}{4\mu_s\mu_v} \qquad (17)$$

where
$\tau_r$ = Rayleigh optical thickness
$P_r(\Theta)$ = Rayleigh scattering phase function
$\mu_v$ = Cosine of viewing angle
$\mu_s$ = Cosine of solar zenith angle

We assume that the atmospheric reflectance due to particle, $R_a$, is also linear with the $\tau_a$ [King, et al., (1999) and Fukushima, et al., (2000)]. This assumption is valid because Liu, et al., (1996) also found linear relationship for both aerosol and molecule scatterings.

$$R_a = \frac{\tau_a P_a(\Theta)}{4\mu_s\mu_v} \qquad (18)$$

where

$\tau_a$ = Aerosol optical thickness
$P_a(\Theta)$ = Aerosol scattering phase function

Atmospheric reflectance is the sum of the particle reflectance and molecule reflectance, $R_{atm}$, (Vermote, et al., 1997).

$$R_{atm} = R_a + R_r \qquad (19)$$

where
$R_{atm}$ = atmospheric reflectance
$R_a$ = particle reflectance
$R_r$ = molecule reflectance

$$R_{atm} = \left| \frac{\tau_a P_a(\Theta)}{4\mu_s\mu_v} + \frac{\tau_r P_r(\Theta)}{4\mu_s\mu_v} \right|$$

$$R_{atm} = \frac{1}{4\mu_s\mu_v}\left[\tau_a P_a(\Theta) + \tau_r P_r(\Theta)\right] \qquad (20)$$

The optical depth is given by Camagni and Sandroni, (1983), as in equation (21). From the equation, we rewrite the optical depths for particle and molecule as equations (22)

$$\tau = \sigma\rho s \qquad (21)$$

where
$\tau$ = optical depth
$\sigma$ = absorption
$s$ = finite path

$$\tau = \tau_a + \tau_r \qquad \text{(Camagni and Sandroni,}$$
1983).

$$\tau_r = \sigma_r\rho_r s \qquad (22a)$$
$$\tau_p = \sigma_p\rho_p s \qquad (22b)$$

Equations (22) are substituted into equation (20). The result can be extended to a three-band algorithm as equation (21)

Equation (21) shows that PM10 is linearly related to the reflectance. This algorithm was generated based on the linear relationship between $\tau$ and reflectance. Retalis et al., (2003), also found that the PM10 was linearly related to the $\tau$ and the correlation coefficient for linear was better than that from the exponential relationship. This means that reflectance was linear with the PM10.

$$R_{atm} = \frac{1}{4\mu_s\mu_v}\left[\sigma_a\rho_a s P_a(\Theta) + \sigma_r\rho_r s P_r(\Theta)\right]$$

$$R_{atm} = \frac{s}{4\mu_s\mu_v}\left[\sigma_a\rho_a P_a(\Theta) + \sigma_r\rho_r P_r(\Theta)\right]$$

$$R_{atm}(\lambda_1) = \frac{s}{4\mu_s\mu_v}\left[\sigma_a(\lambda_1)PP_a(\Theta,\lambda_1) + \sigma_r(\lambda_1)GP_r(\Theta,\lambda_1)\right]$$

$$R_{atm}(\lambda_2) = \frac{s}{4\mu_s\mu_v}\left[\sigma_a(\lambda_2)PP_a(\Theta,\lambda_2) + \sigma_r(\lambda_2)GP_r(\Theta,\lambda_2)\right]$$

$$P = a_0 R_{atm}(\lambda_1) + a_1 R_{atm}(\lambda_2) \qquad (21)$$

Where
P = Particle concentration (PM10)
G = Molecule concentration
$R_{atmi}$ = Atmospheric reflectance, i = 1 and 3 are the band number
$a_j$ = algorithm coefficients, j = 0, 1, 2, … are then empirically determined.

### 2.3.2 Land Cover

Besides that, we also successfully map the land cover by using satellite ALOS data. In this project, an algorithm

was developed to generate the water quality map over Penang Island, Malaysia.

Three supervised classification methods were performed to the digital satellite image - Maximum Likelihood, Minimum Distance-to-Mean, and Parallelepiped. Three unsupervised classification methods used were K-means, Fuzzy K-Means, and Isodata.

## 1. DATA ANALYSIS AND RESULTS

### 3.1 Conversion from DN to absolute scale

Remote sensing satellite detectors exhibit linear response to incoming radiance, whether from the Earth's surface radiance or internal calibration sources. This response is quantized into 8-bit values that represent brightness values commonly called Digital Numbers (DN). To convert the calibrated digital numbers to at-aperture radiance, rescaling gains and biases are created from the known dynamic range limits of the instrument. And then, the spectral radiance, as calculated above, was converting to a sensor reflectance values.

The AVNIR-2 products are processed into CEOS format, and external ASCII file ('summary.txt') is embedded within the product. The rescaling gain and offset are not directly written into 'summary file' but only into scene header record. The rescaling gain and offset is changing along with time and geographical position.

Radiance, $L(\lambda) = \text{Bias}(\lambda) + [\text{Gain}(\lambda) \times DN(\lambda)]$   (20)

where

$\lambda$ = band number.

L is the radiance expressed in $\text{Wm}^{-2}\,\text{sr}^{-1}\mu\text{m}^{-1}$.

$$\rho^* = \frac{\pi L(\lambda)d^2}{E_0(\lambda)\cos\theta} \qquad (21)$$

Where

$\rho^*$ = Sensor Reflectance values
$\pi$ = 22/7
$L(\lambda)$ = Apparent At-Sensor Radiance ($\text{Wm}^{-2}\,\text{sr}^{-1}\mu\text{m}^{-1}$)

$d$ = Earth-Sun distance in astronomical units
= $\{1.0-0.016729\cos[0.9856(D-4)]\}$ where (D = day of the year)
$E_0(\lambda)$ = mean solar exoatmospheric irradiance ($\text{Wm}^{-2}\,\mu\text{m}^{-1}$)
$\theta$ = solar Zenith angle (degrees)

Table 3: Rescaling gains and biases used for the conversion of L1 calibrated digital numbers to spectral radiance for ALOS AVNIR-2.

| ALOS AVNIR-2 | | |
|---|---|---|
| BAND | Grescale | Brescale |
| 1 | 0.5880 | 0.0000 |
| 2 | 0.5730 | 0.0000 |
| 3 | 0.5020 | 0.0000 |
| 4 | 0.8350 | 0.0000 |

Table 4: Solar Exoatmospheric spectral irradiances in $Wm^{-2}\,\mu m^{-1}$.

| ESUN | |
|---|---|
| BAND | ALOS |
| 1 | 1943.3 |
| 2 | 1813.7 |
| 3 | 1562.3 |
| 4 | 1076.5 |

### 3.2 Water Quality Map

A simple atmospheric correction of darkest pixel technique was performed in this study. This is a very simple correction, based on 2 assumptions:
• The first assumption is that in the darkest water pixel of the image there is total light absorption i.e. this pixel represents black water and the light recorded for this pixel is equal to the atmospheric path radiance.
• Secondly it is assumed that the atmospheric path radiance is uniform all over the image. The spectrum of the darkest water pixel (assumed to represent the atmosphere) is subtracted from the whole image. The darkest pixel is found by searching for the lowest values over water for all wavelengths. The pixel with the lowest value in most of the bands was selected as the darkest pixel.

Image rectification was performed by using a second order polynomial tranformation equation. The images were geometrically corrected by using a nearest

neighbour resampling technique. Sample locations were then identified on these geocoded images. Regression technique was employed to calibrate the algorithm using the satellite multispectral signals.

The DNs corresponding to the water sample locations were extracted from all of the images. To reduce data noise average DN values were calculated. For each scene, sets of data were extracted by using different window sizes and those data sets were then tested with our model. The window size (array) that resulted in the highest accuracy was selected as the average filter for that scene. And then the digital numbers for each band corresponding to the sea-truth locations were extracted and then converted into radiance values and reflectance values. Data distribution characteristics were used to determine the validity of the proposed algorithm for fitting the data.

In this study, the reflectances derived from ALOS AVIR-2 signals were used as independent variables in our calibration regression analyses for TSS. The accuracy was determined from the correlation coefficient (R) and root-mean-squares (RMS) values. The proposed developed algorithm produced a high correlation coefficient of 0.9125 and low RMS value of 9.26548 (mg/l). The PM10 maps were generated using the proposed algorithm. Finally the PM10 map was geometrically corrected and colour-coded for visual interpretation (Figure 6 and Figure 7).
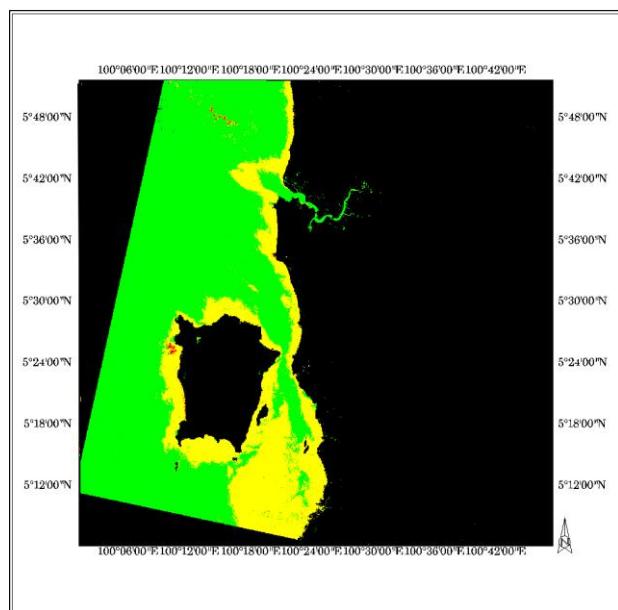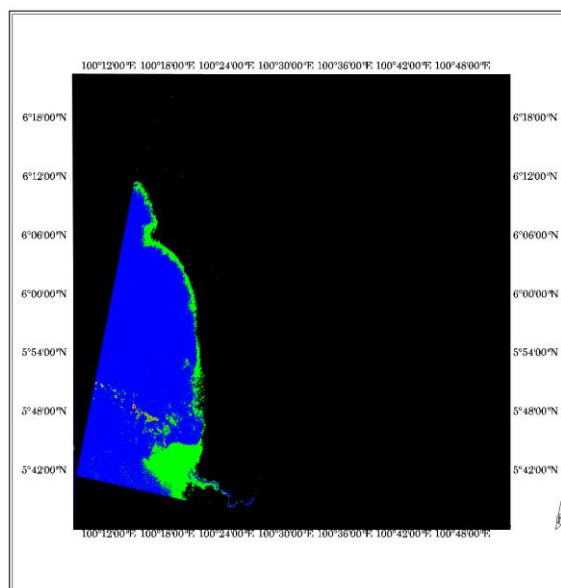


**Fig. 7 Map of TSS around Yan, Kedah (Blue = (< 101) mg/l, Green = (100-150) mg/l, Yellow = (151-200) mg/l, Orange = (200-250) mg/l, red = (>250) mg/l, Brown = Land and Black = Area outside image)**

## 3.3 Air quality Map

The ALOS-AVNIR-2 satellite data used in this study was captured on 24 April 2007. Over a dark target, the observed atmospheric reflectance can be written as a simple sum of reflectance from aerosols and Rayleigh contributions. This simplification, however, is not valid at short wavelengths (less than 0.45 pm) or large sun and view zenith angles (Vermote and Roger, 1996). We can obtain the atmospheric reflectance values by subtracting surface reflectance (by taking account of the atmospheric transmittance) from the amount of reflectance measured from the satellite [reflectance at the top of atmospheric, $\rho$(TOA)] (Popp, et al. 2004), (Equation 22).

$$R_s - R_r = R_{atm} \tag{22}$$

where
$R_s$ = reflectance recorded by satellite sensor.
$R_r$ = reflectance from surface references.
$R_{atm}$ = reflectance from atmospheric components (aerosols and molecules).

Then the digital numbers for the three visible bands were converted to radiance and reflectance values. It should be noted that the relfectance values at the top of atmospheric was the sum of the surface reflectance and atmospheric relfectance. In this study, we are using ACTOR2 image correction software in the PCI Geomatica 9.1 image processing software for creating a surface reflectance image. And then the reflectance measured from the satellite [reflectance at the top of



**Fig. 6 Map of TSS around Penang Island, Malaysia (Blue = (< 100) mg/l, Green = (100-150) mg/l, Yellow = (151-200) mg/l, Orange = (200-250) mg/l, red = (>250) mg/l, Brown = Land and Black = Area outside image)**

atmospheric, ρ(TOA)] was subtracted by the amount given by the surface reflectance to obtain the atmospheric reflectance. And then the atmospheric reflectance was related to the PM10 using the regression algorithm analysis.

In this study, ALOS-AVNIR-2 signals were used as independent variables in our calibration regression analysis. The atmospheric reflectance values were combined and related to the corresponding PM10 values. The data were used for algorithm calibration. The coefficients of the calibrated algorithm were determined by using regression technique. PM10 maps were generated using the proposed calibrated algorithm.

Then, colour-coded maps were produced for visual interpretation and geometrically corrected for displaying distribution patterns of PM10 over the land and PM10 map over the water areas as shown in Figures 1 and 2 respectively. Generally, PM10 concentrations in the industrial and urban areas were higher compared to other areas based on the generated PM10 map.

The accuracy was determined from the correlation coefficient (R) and root-mean-squares (RMS) values. The proposed developed algorithm produced a high correlation coefficient of 0.8599 and low RMS value of 10.5886 (µg/m$^3$). The PM10 maps were generated using the proposed algorithm. Finally the PM10 map was geometrically corrected and colour-coded for visual interpretation (Figure 8 and Figure 9).

High air pollution levels also originated from stationary sources such as the chemical and manufacturing industries. Further more, there are many mobile sources such as motor vehicles that cause the PM10 concentrations to be high in the urban area. The particles and dust in Penang, Malaysia mostly come from the motor vehicles, smoke from forest fires in the neighbouring country, and particles/dust generated from the industrial activities.
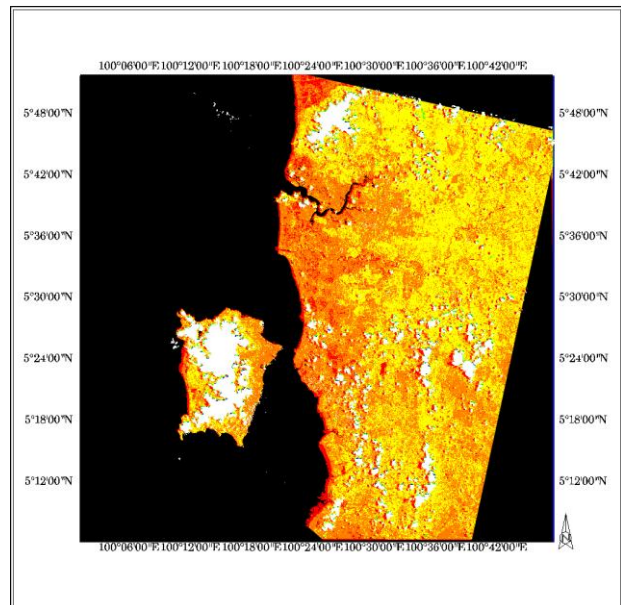


**Fig. 8 Map of PM10 around Yan, Kedah, Malaysia [Yellow < 50 µg/m3, Orange = (50-100) µg/m3, Red = (>100) µg/m3, Blue and Green = Cloud and Black = Water and Area outside the image]**
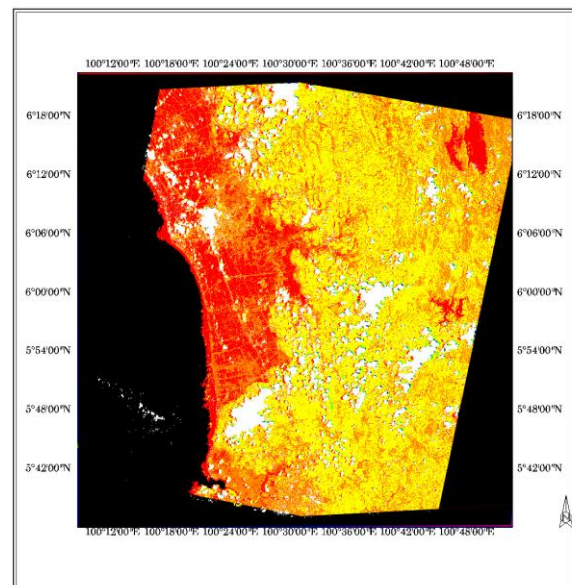


**Fig. 9 Map of PM10 around Yan, Kedah, Malaysia [Yellow < 50 µg/m3, Orange = (50-100) µg/m3, Red = (>100) µg/m3, Blue and Green = Cloud and Black = Water and Area outside the image]**

**3.4        Land Cover Map**

All image-processing tasks were carried out using PCI Geomatica version 9.1.8 digital image processing software at the School Of Physics, Universiti Sains Malaysia (USM). The satellite image was then

geometrically corrected by second order polynomial equation using the nearest neighbor method. Figure 2 shows the raw satellite image.

The aim of the classification analysis is to categorize all the pixels in the digital camera imagery into land cover classes. The satellite image was classified using three supervised classification methods with a set of the training data set. The mosaic digital image was classified into 4 classes using three visible bands (Vegetation, Urban, Water and cloud). The available ground truth data were used in the accuracy assessment analysis for the classified map. The accuracy of the classified map was analysed using confusion matrix and Kappa coefficient.

The areas were established using polygons. They are delineated by spectrally homogeneous sub areas, which have, class name given. A total of 35 sample-training areas were studied in this analysis. Once the training sites and classes were assigned, the images were then classified using the three supervised classification methods (Maximum Likelihood, Minimum Distance-to-Mean, Parallelepiped and Neural Network). Accuracy assessment was carried out to compute the probability of error for each classified map. The overall accuracy is expressed as a percentage of the test-pixels successfully assigned to the correct classes.

The frequency based contextual classifier performs classification of multispectral imagery using a grey level reduced image and a set of training site bitmaps. The frequency based contextual classifier performs the second of two steps in frequency-based contextual classification of multispectral imagery. It inputs a grey level vector reduction image (must be 8-bit layer) and a set of training site bitmap layers, and creates a classification image under the specified output window. Each input bitmap can be assigned a unique output class value for the classification image. The contextual classifier uses a pixel window of specified size around each pixel.

The classified map produced by each classifier was checked with the confusion or error matrix and Kappa statistic. The results obtained are presented in Table 1. The high Kappa coefficient suggests a good relationship between the classified image and the reference data. The assessment results showed a reasonably good agreement between the land cover data set and the reference data. The overall classification accuracy achieved by the neural network classifier for categorizing land cover for Kedah, Malaysia was shown in Table 5 and Table 6. The classified land cover maps using Neural Network are shown in Figure 11 and Figure 12.
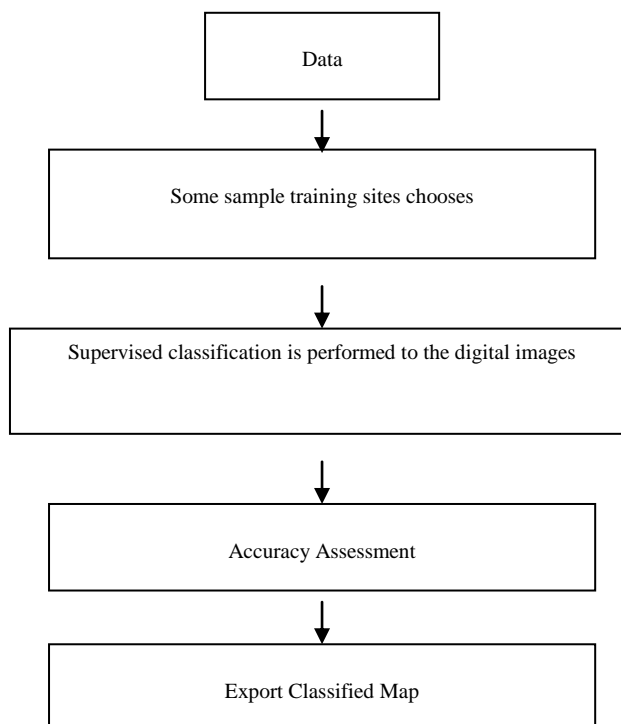


**Fig. 10 Flow chart for data processing of the images**

**Table 5. The overall classification accuracy and Kappa coefficient**

| Classification method | Kappa coefficient | | Overall classification accuracy (%) | |
|---|---|---|---|---|
| | Kedah, Malaysia | Penang Island, Malaysia | Kedah, Malaysia | Penang Island, Malaysia |
| Maximum Likelihood | 0.8952 | 0.8535 | 90.65 | 86.36 |
| Minimum Distance-to-Mean | 0.7582 | 0.6221 | 75.26 | 60.15 |
| Parallelepiped | 0.5962 | 0.6212 | 60.25 | 69.85 |
| Parallelepiped (with Maximum Likelihood Tie Resolution) | 0.9252 | 0.8723 | 91.68 | 88.36 |
| Neural network | 0.9368 | 0.9159 | 93.23 | 91.25 |

**Table 6. The overall classification accuracy and Kappa coefficient**

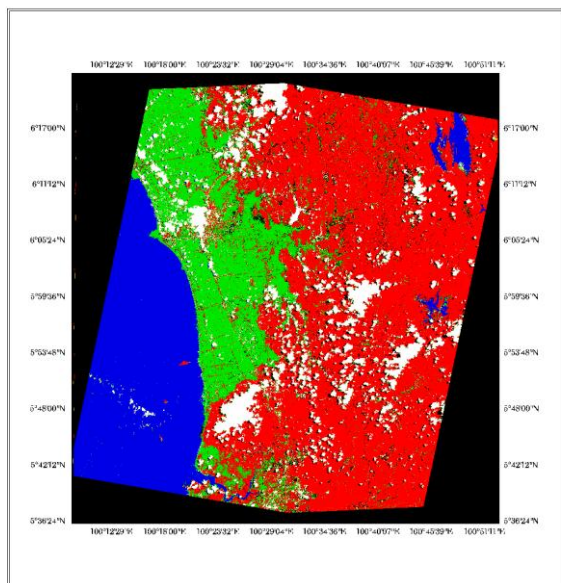| Classification method | Contextual classifier | |
|---|---|---|
| | Kedah, Malaysia | Penang Island, Malaysia |
| Kappa coefficient | 0.9782 | 0.96219 |
| Overall classification accuracy (%) | 96.36 | 95.51 |



**Fig. 11 The land cover map using ALOS AVNIR image [Colour Code: Green = wet land, Blue = Water, Red = Vegetation, White = Cloud and Black = Area outside the image]**
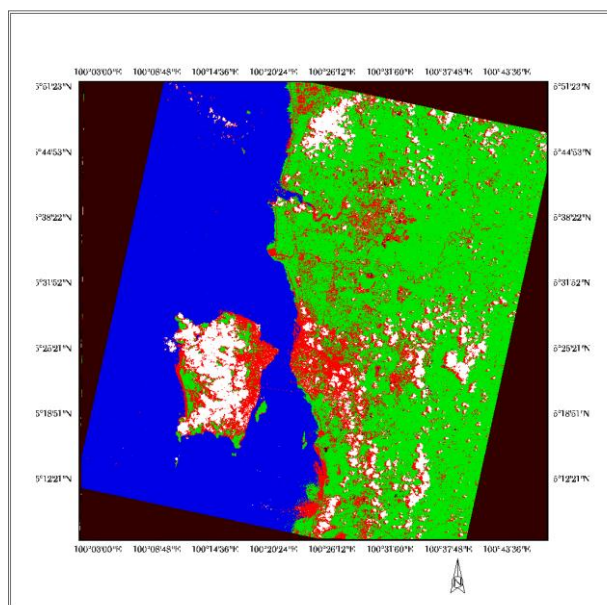


**Fig. 12. The land cover map using ALOS image [Colour Code: Red = urban, Green = Vegetation, Blue = Water, White = Cloud and Black = Area outside the image]**

The ASF MapReady program from Alaska satellite Facility Geographical Institute at the University of Alaska Fairbanks was used to convert raw PALSAR data into georeferenced files. The free software was downloaded from the ASF website. To process the radar imagery effectively and efficiently, we applied a radiometric and geometric correction to the ALOS PALSAR data acquired on 25 May 2007. For analyzing the synergistic effects of SAR data with different polarization and incident angles it is essential to work with geometric highly referenced data. After converting DN to Sigma-nought to obtain radar backscattering coefficients, we calculated a geometric terrain correction using DEM data to prevent relief displacement. DN values were converted to sigma-nought to obtain radar backscattering coefficients. Geocoded ALOS-PALSAR L-band polarimetric data with 12.5m spatial resolution and 21.5 degree incident angle recorded on 25 May 2007 was used in this study.

Water is expected to produce a low backscatter values (sigma-nought) because its acts in a specular manner, reflecting energy away from sensor. Paddy also has a low backscatter values. This is because the imagery captured was during sowing season, and all the paddy have not fully matured. Bare land acts like a specular manner, so the backscatter values are comparatively low. Urban areas indentified in this study site are within Bayan Lepas (industrial area) and hence are heavily urbanized. They show high backscatter values.

Different mean backscatter values and their standard deviations were observed across the four bands.

The VV and HH (bands 1 and 4) show much higher values for all four land cover/uses when compared to the HV and VH (bands 2 and 3).

In this study, Variance texture measures are extract at the different window sizes (5x5, 7x7, and 11x11) for each band of the PALSAR data. Seven primary land covers/uses were determined and their spectral signatures were extracted from original and the texture data. Transformed Divergence (TD) separability measures were then calculated to identify the probability of correct classification of classes. Table 2 summarizes the TD values for the radar datasets. The separability for all class pairs, with the exception of a few pairs, is satisfactory. There is a room for improvement these TD values by using texture measures.

Prior to the data analysis, it is essential to examine the statistical values for the data. Mean and standard deviation for area of interest (AOIs) were extracted and are presented in Table 6.

Variance textures measure for different window sizes (5 x 5, 7 x 7 and 11 x 11) were calculated for each PALSAR data bands. TD values for each of the textures were calculated for all land cover/use pairs (Table 2). All land cover/use pairs indicate an overall improvement with the texture TD over the original backscatter TD values. Besides, we can conclude that as the window size increased, the TD values improved. The 7 x 7 texture provides superior results for TD values. The 7 x 7 texture TD shows significant improvement over the original TD for the PALSAR image.

Fusions of the original radar data with the three texture sizes were tested. The result shows that the highest of TD values were achieved by fusing the 7 x 7 texture band with the original radar (Table 4). When fusing the original PALSAR image and the 7 x 7 texture bands into a single analysis, the new TD values for the HV and VH polarizations are excellent (Table 5). The TD values for the HH and VV polarizations, shows substantial improvements over the original components, but do not perform as well as the HV and VH polarizations in fusion of the original image and 7 x 7 texture windows.

**Table 6. AOI class statistics from PALSAR data (mean/standard deviation)**

| Land Cover / use classes | | HH | HV | VH | VV |
|---|---|---|---|---|---|
| | | | Bands | | |
| Water | Mean | -11.402 | -28.072 | -27.621 | -9.987 |
| | SD | 2.339 | 1.136 | 1.429 | 2.426 |
| Urban | Mean | -6.941 | -10.296 | -10.925 | -7.283 |
| | SD | 6.11 | 6.173 | 6.155 | 6.347 |
| Forest | Mean | -10.821 | -16.347 | -16.963 | -11.3 |
| | SD | 8.613 | 9.964 | 10.137 | 8.427 |
| Oil Palm | Mean | -8.864 | -16.166 | -16.695 | -10.537 |
| | SD | 2.13 | 2.083 | 2.093 | 2.117 |
| Bare Land | Mean | -13.878 | -24.761 | -24.895 | -14.49 |
| | SD | 5.063 | 6.383 | 6.378 | 3.575 |
| Paddy | Mean | -13.834 | -25.712 | -25.435 | -17.902 |
| | SD | 3.586 | 2.053 | 2.017 | 3.676 |
| Residential | Mean | -4.128 | -12.214 | -12.725 | -7.075 |
| | SD | 3.086 | 3.7 | 3.715 | 2.675 |

**Table 7. TD values for Original backscatter values for PALSAR image**

| Separability | Polarization | | | |
|---|---|---|---|---|
| | HH | HV | VH | VV |
| Bare Land -Water | 408 | 1569 | 1390 | 493 |
| Forest -Bare Land | 216 | 430 | 406 | 410 |
| Forest-Water | 1035 | 2000 | 1997 | 959 |
| Oil palm -Bare Land | 878 | 1623 | 1573 | 522 |
| Oil palm-Forest | 1229 | 1438 | 1461 | 1166 |
| Oil palm-Water | 303 | 1998 | 1990 | 23 |
| Paddy-Bare Land | 49 | 702 | 720 | 245 |
| Paddy-Forest | 511 | 1860 | 1847 | 679 |
| Paddy-Oil palm | 818 | 1854 | 1785 | 1304 |
| Paddy-Water | 264 | 557 | 433 | 1237 |
| Residential -Bare Land | 823 | 574 | 564 | 884 |
| Residential-Forest | 663 | 96 | 125 | 957 |
| Residential-Oil palm | 567 | 824 | 1776 | 415 |
| Residential-Paddy | 1010 | 1830 | 1798 | 1528 |
| Residential-Water | 985 | 1999 | 1997 | 242 |
| Urban-Bare Land | 86 | 633 | 607 | 81 |
| Urban-Forest | 256 | 1994 | 233 | 243 |
| Urban-Oil palm | 400 | 551 | 514 | 317 |
| Urban-Paddy | 145 | 1779 | 1772 | 504 |
| Urban-Residential | 476 | 20 | 19 | 494 |
| Urban-Water | 210 | 2000 | 1991 | 249 |

**Table 8. TD values for three variance texture windows for PALSAR image (a) 3x3 texture, (b) 5x5 texture, (c) 7x7 texture**

| Separability | Polarization | | | |
|---|---|---|---|---|
| | HH | HV | VH | VV |
| TD values　（3x3 texture） | | | | |
| Bare Land -Water | 2000 | 2000 | 2000 | 124 |
| Forest -Bare Land | 258 | 1024 | 946 | 248 |
| Forest-Water | 1916 | 2000 | 2000 | 25 |
| Oil palm -Bare Land | 2000 | 2000 | 2000 | 113 |
| Oil palm-Forest | 1912 | 1970 | 1980 | 22 |
| Oil palm-Water | 3 | 1000 | 822 | 4 |
| Paddy-Bare Land | 1344 | 2000 | 2000 | 826 |
| Paddy-Forest | 414 | 1980 | 1995 | 138 |
| Paddy-Oil palm | 843 | 11 | 17 | 282 |
| Paddy-Water | 870 | 810 | 610 | 262 |
| Residential -Bare Land | 1495 | 1627 | 1466 | 394 |
| Residential-Forest | 505 | 100 | 74 | 22 |

| Residential-Oil palm | 829 | 1639 | 1758 | 76 |
|---|---|---|---|---|
| Residential-Paddy | 8 | 1697 | 1878 | 63 |
| Residential-Water | 863 | 2000 | 2000 | 63 |
| Urban-Bare Land | 912 | 1983 | 1980 | 54 |
| Urban-Forest | 155 | 465 | 495 | 63 |
| Urban-Oil palm | 1505 | 1201 | 1252 | 9 |
| Urban-Paddy | 102 | 1308 | 1489 | 413 |
| Urban-Residential | 116 | 140 | 195 | 143 |
| Urban-Water | 1528 | 1998 | 1998 | 17 |

(a)

| Separability | Polarization | | | |
|---|---|---|---|---|
| | HH | HV | VH | VV |
| TD values ( 5x5 texture ) | | | | |
| Bare Land –Water | 2000 | 2000 | 539 | 15 |
| Forest –Bare Land | 26 | 272 | 470 | 49 |
| Forest-Water | 2000 | 2000 | 85 | 24 |
| Oil palm –Bare Land | 2000 | 2000 | 110 | 24 |
| Oil palm-Forest | 2000 | 2000 | 129 | 5 |
| Oil palm-Water | 96 | 1030 | 242 | 16 |
| Paddy-Bare Land | 1129 | 2000 | 347 | 308 |
| Paddy-Forest | 1247 | 2000 | 65 | 139 |
| Paddy-Oil palm | 1836 | 16 | 71 | 196 |
| Paddy-Water | 1345 | 882 | 286 | 186 |
| Residential –Bare Land | 1270 | 1545 | 270 | 59 |
| Residential-Forest | 1388 | 680 | 32 | 16 |
| Residential-Oil palm | 1776 | 1987 | 57 | 26 |
| Residential-Paddy | 4 | 1961 | 91 | 93 |
| Residential-Water | 1251 | 2000 | 60 | 15 |
| Urban-Bare Land | 832 | 1983 | 572 | 12 |
| Urban-Forest | 863 | 1492 | 36 | 13 |
| Urban-Oil palm | 1993 | 1942 | 220 | 2 |
| Urban-Paddy | 122 | 1883 | 200 | 225 |
| Urban-Residential | 161 | 194 | 48 | 31 |
| Urban-Water | 1852 | 2000 | 14 | 11 |

(b)

| Separability | Polarization | | | |
|---|---|---|---|---|
| | HH | HV | VH | VV |
| TD values ( 7x7 texture ) | | | | |
| Bare Land -Water | 2000 | 2000 | 2000 | 520 |
| Forest -Bare Land | 228 | 747 | 686 | 425 |
| Forest-Water | 2000 | 2000 | 2000 | 965 |
| Oil palm -Bare Land | 2000 | 2000 | 2000 | 530 |
| Oil palm-Forest | 1999 | 2000 | 2000 | 221 |
| Oil palm-Water | 1339 | 2000 | 2000 | 708 |
| Paddy-Bare Land | 50 | 1024 | 902 | 250 |

| | | | | |
|---|---|---|---|---|
| Paddy-Forest | 673 | 2000 | 2000 | 679 |
| Paddy-Oil palm | 1315 | 1990 | 85 | 1304 |
| Paddy-Water | 1216 | 864 | 707 | 1239 |
| Residential -Bare Land | 1539 | 1606 | 1462 | 884 |
| Residential-Forest | 852 | 214 | 177 | 981 |
| Residential-Oil palm | 1228 | 1888 | 1934 | 490 |
| Residential-Paddy | 1090 | 1874 | 1971 | 1528 |
| Residential-Water | 1138 | 2000 | 2000 | 264 |
| Urban-Bare Land | 982 | 1987 | 1990 | 85 |
| Urban-Forest | 353 | 1964 | 852 | 267 |
| Urban-Oil palm | 1840 | 1609 | 1615 | 412 |
| Urban-Paddy | 145 | 1779 | 1764 | 510 |
| Urban-Residential | 476 | 168 | 248 | 500 |
| Urban-Water | 1781 | 2000 | 2000 | 270 |

(c)


**Table 9. TD value is achieved by fusion the 7 x 7 texture band with the original radar**

| Separability | Polarization | | | |
|---|---|---|---|---|
| | HH | HV | VH | VV |
| Bare Land -Water | 2000 | 2000 | 2000 | 572 |
| Forest -Bare Land | 563 | 1268 | 1217 | 570 |
| Forest-Water | 2000 | 2000 | 2000 | 973 |
| Oil palm -Bare Land | 2000 | 2000 | 2000 | 593 |
| Oil palm-Forest | 2000 | 2000 | 2000 | 1207 |
| Oil palm-Water | 328 | 2000 | 1994 | 52 |
| Paddy-Bare Land | 1366 | 2000 | 2000 | 879 |
| Paddy-Forest | 1150 | 2000 | 2000 | 785 |
| Paddy-Oil palm | 1603 | 1866 | 1800 | 1470 |
| Paddy-Water | 1350 | 1087 | 911 | 1332 |
| Residential -Bare Land | 1780 | 1836 | 1754 | 1077 |
| Residential-Forest | 1436 | 518 | 497 | 984 |
| Residential-Oil palm | 1503 | 1949 | 1972 | 490 |
| Residential-Paddy | 1075 | 1984 | 1996 | 1568 |
| Residential-Water | 1636 | 2000 | 2000 | 303 |
| Urban-Bare Land | 1055 | 1993 | 1994 | 116 |
| Urban-Forest | 567 | 940 | 1054 | 313 |
| Urban-Oil palm | 1869 | 1742 | 1748 | 334 |
| Urban-Paddy | 251 | 1933 | 1953 | 876 |
| Urban-Residential | 706 | 186 | 261 | 618 |
| Urban-Water | 1821 | 2000 | 2000 | 282 |

**Table 10. Different between TD values of original and fusion original and 7x7 texture**

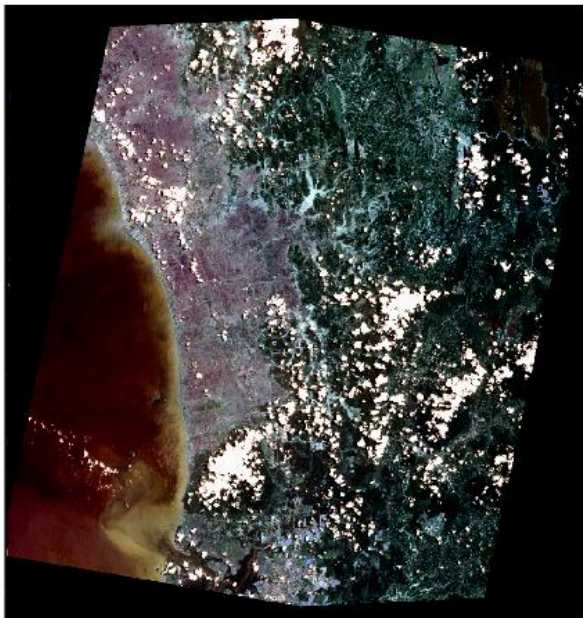| Separability | Polarization | | | |
|---|---|---|---|---|
| | HH | HV | VH | VV |
| Bare Land -Water | +1592 | +431 | +610 | +79 |
| Forest -Bare Land | +347 | +838 | +811 | +160 |
| Forest-Water | +965 | 0 | +3 | +14 |
| Oil palm -Bare Land | +1122 | +377 | +427 | +71 |
| Oil palm-Forest | +771 | +562 | +539 | +41 |
| Oil palm-Water | +25 | +2 | +4 | +29 |
| Paddy-Bare Land | +1317 | +1298 | +1280 | +634 |
| Paddy-Forest | +639 | +140 | +153 | +106 |
| Paddy-Oil palm | +785 | +12 | +15 | +166 |
| Paddy-Water | +1086 | +530 | +478 | +95 |
| Residential -Bare Land | +957 | +1262 | +1190 | +193 |
| Residential-Forest | +773 | +422 | +372 | +27 |
| Residential-Oil palm | +936 | +1125 | +196 | +75 |
| Residential-Paddy | +65 | +154 | +198 | +40 |
| Residential-Water | +651 | +1 | +3 | +61 |
| Urban-Bare Land | +969 | +1360 | +1387 | +35 |
| Urban-Forest | +311 | +1054 | +821 | +70 |
| Urban-Oil palm | +1469 | +1191 | +1234 | +17 |
| Urban-Paddy | +106 | +154 | +181 | +372 |
| Urban-Residential | +230 | +166 | +242 | +124 |
| Urban-Water | +1611 | 0 | +9 | +33 |

The original PALSAR data were limited in their capability to separate land cover/use for the Penang Island scene. The extraction and calculation of Variance texture measures for each radar polarization resulted in consistently improved TD values. As the window size of the texture measure increased, the TD values improved. Fusing the original PALSAR image with the best of the texture images provided excellent TD values, implying excellent separability for classification. The results of this study show that texture measures extracted from quad-polarization radar data greatly improve separability between different land cover/use classes, suggesting that the use of radar texture measures will help to improve overall classification accuracy.

## 2. DISCUSSION AND PROSPECTS

Basically, this project was archived the research objectives and the target that we set before throughout the research in the phase I (by the time of this interim report). All the milestones of this project were also archived throughout the research in the phase I. Everything was following the original research plan. In this project, the environmental changes parameters that we set before were water quality and land cover features only, but we also tested the ALOS data for air quality studied. And we obtained very promising results from this project. The TSS and PM10 retrieved from the algorithm shown high accuracies. The developed algorithm produced high R and low RMS values. The result produce by this study indicated the used of ALOS satellite image for studying environmental changes of water quality, air quality and land cover changes over Penang Island, Malaysia. In the phase II, we will detailed

interpret the retrieved information by using ALOS satellite data. We still will continuous to study the water quality and air quality by using ALOS data. The feasibility of applying the present technique for operational use will be further validated in the phase II of this project. Further studies will be conducted to improve the results. We also will study the land cover features mapping by using other classification (Neural Network and Frequency Based Classification Techniques) over Penang, Malaysia. We will test the used of ALOS satellite data for turbidity mapping instead of TSS only and mangrove mapping in the phase II of this project. Besides that, we also will use the Panchromatic Remote-sensing Instrument for Stereo Mapping (PRISM) of ALOS satellite data to retrieve a highly accurate digital elevation model (DSM) over Penang.

**List of data used in the research**
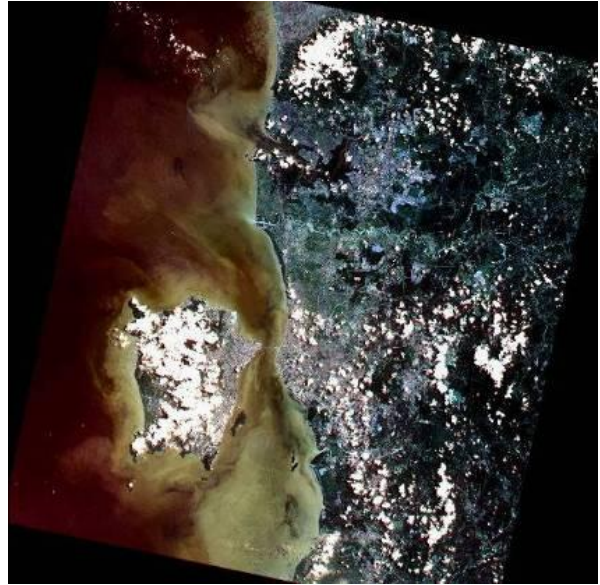


Raw satellite image used in this study over Kedah, Malaysia.



Raw satellite image used in this study over Penang Island, Malaysia.



Raw ALOS-PALSAR image used in this study over Penang, Malaysia.

In situ of PM10 and TSS over Penang Island, Malaysia

| Longitude | Latitude | PM10 |
|---|---|---|
| 100.3086 | 5.385225 | 85 |
| 100.3142 | 5.396614 | 95 |
| 100.3295 | 5.408836 | 101 |
| 100.3417 | 5.416614 | 123 |
| 100.3228 | 5.424114 | 97 |
| 100.2908 | 5.465225 | 86 |
| 100.2411 | 5.461614 | 58 |
| 100.205 | 5.415781 | 51 |
| 100.2231 | 5.302725 | 58 |
| 100.2603 | 5.293281 | 102 |
| 100.2895 | 5.321892 | 124 |
| 100.3083 | 5.366058 | 87 |

| Longitude | Latitude | TSS |
|---|---|---|
| 100.3656 | 5.408003 | 125 |
| 100.3506 | 5.387447 | 96 |
| 100.3303 | 5.392169 | 101 |
| 100.3328 | 5.362447 | 85 |
| 100.3708 | 5.377725 | 124 |
| 100.3583 | 5.357725 | 86 |
| 100.3683 | 5.330225 | 95 |
| 100.342 | 5.290225 | 125 |
| 100.3072 | 5.321614 | 95 |
| 100.3347 | 5.330503 | 86 |
| 100.3192 | 5.351892 | 85 |
| 100.3181 | 5.368011 | 89 |

In situ of PM10 and TSS over Kedah, Malaysia

| Longitude | Latitude | PM10 |
|---|---|---|
| 100.9507 | 5.630611 | 101 |
| 100.5824 | 5.367611 | 86 |
| 100.324 | 5.468444 | 78 |
| 100.5106 | 5.777 | 68 |
| 100.9266 | 5.719444 | 59 |
| 100.1944 | 5.055167 | 49 |
| 100.2756 | 5.518611 | 51 |
| 100.1225 | 5.668889 | 53 |
| 100.7782 | 5.037611 | 77 |

| Longitude | Latitude | TSS |
|---|---|---|
| 100.3463 | 5.665 | 112 |
| 100.7977 | 5.348833 | 74 |
| 100.1664 | 5.734111 | 82 |
| 100.3866 | 5.542889 | 86 |
| 100.1999 | 5.279889 | 75 |
| 100.3148 | 5.093444 | 92 |
| 100.7642 | 5.165222 | 108 |
| 100.8406 | 5.720111 | 136 |
| 100.4723 | 5.868444 | 85 |
| 100.324 | 5.279889 | 121 |
| 100.4723 | 5.619444 | 102 |

**Papers published in the research**

(1) H. S. Lim, M. Z. MatJafri, K. Abdullah and N. Mohd. Saleh, 2007, Land cover mapping over Penang Island, Malaysia based on frequency-based contextual classification, *Proceeding of the The First Joint PI Symposium of ALOS Data Nodes for ALOS Science Program in Kyoto*, Kyoto, Japan. Available Online: http://www.eorc.jaxa.jp/ALOS/conf/Proc_PIsymp2007/contents/absentee_proceedings/LUG10.pdf.

(2) H. S. Lim, M. Z. MatJafri, K. Abdullah and N. Mohd. Saleh, 2007, High spatial resolution land cover mapping using ALOS data over Penang Island, Malaysia, *Proceeding of the The First Joint PI Symposium of ALOS Data Nodes for ALOS Science Program in Kyoto*, Kyoto, Japan. Available Online: http://www.eorc.jaxa.jp/ALOS/conf/Proc_PIsymp2007/contents/absentee_proceedings/LUG09.pdf.

(3) H. S. Lim, M. Z. MatJafri, K. Abdullah, A. N. Alias and N. Mohd. Saleh, 2008, Application of ALOS Imagery to Estimate Total Suspended Solids (TSS) over Penang Island, Malaysia, *Proceeding of the International Symposium and Exhibition on Geoinformation 2008 (ISG 2008) (Proceeding in CD)*, Kuala Lumpur, Malaysia.

(4) C. J. Wong, M. Z. MatJafri, K. Abdullah and H. S. Lim, 2009, Temporal and Spatial Air Quality Monitoring Using Internet Surveillance Camera and ALOS Satellite Image, *Proceeding of the 2009 IEEE Aerospace Conference*, Big Sky, Montana, USA. p.p. 1 – 7, Digital Object Identifier. 10.1109/AERO.2009.4839318.

(5) C. K. Sim, K. Abdullah, M. Z. MatJafri and H. S. Lim, 2009, Land Cover Mapping using ALOS PALSAR Data over Penang Island, Malaysia, *Proceeding of the Map Malaysia 2009*, Equatorial Hotel, Penang, Malaysia. Available Online: http://gisdevelopment.net/application/nrm/overview/mma09_cksim.htm.

(6) C. E. Joanna Tan, M. Z. MatJafri, K. Abdullah and H. S. Lim, 2009, Generating Digital Elevation Model (DEM) from ALOS-PRISM over Penang Island, Malaysia, *Proceeding of the Map Malaysia 2009*, Equatorial Hotel, Penang, Malaysia.

(7) H. S. Lim, M. Z. MatJafri and K. Abdullah, 2009, Turbidity Measurement from ALOS Satellite Imagery, *Proceeding of the IEEE Oceans'09*, Bremen, Germany. p. p. 1 - 5, Digital Object Identifier 10.1109/OCEANSE.2009.5278185.

(8) M. R. Mustapha, <u>H. S. Lim</u> and M. Z. Mat Jafri, 2009, Land Cover Mapping over Makkah and Mina Using ALOS AVNIR-2 Satellite Image, *Proceeding of the 3rd Asian Physics Symposium 2009,* Bandung, Indonesia. p.p. 215 - 210.

(9) <u>H. S. Lim</u>, M. Z. MatJafri, K. Abdullah and C. J. Wong, 2009, Total Suspended Solids (TSS) Mapping Using ALOS Imagery over Penang Island, Malaysia, *Proceeding of The 6th International Conference Computer Graphics, Imaging and Visualization 2009 (CGIV 2009)***,** Tianjin, China. p.p. 503 - 509. Digital Object Identifier 10.1109/CGIV.2009.39.

(10) C. K. Sim, K. Abdullah, M. Z. MatJafri, and <u>H. S. Lim</u>, 2009, Analysis of Land Cover/Use over Penang Island, Malaysia by Using ALOS PALSAR Data, *Proceeding of The International Conference on Space Science & Communication 2009 (IconSpace 2009),* Port Dickson, Negeri Sembilan, Malaysia. p. p. 209 – 211, Digital Object Identifier :10.1109/ICONSPACE.2009.5352635.

(11) C. K. Sim, K. Abdullah, M. Z. MatJafri and <u>H. S. Lim</u>, 2009, Land Cover Mapping using ALOS PALSAR Data over Penang Island, Malaysia, *Proceeding of the Advanced Technology Congress (ATC) - Conference on Spatial and Computational Engineering, SPACE Section (Proceeding in CD)*, Putra World Trade Centre (PWTC), Kuala Lumpur, Malaysia.

(12) Syazwani Mohd Yusop, Khiruddin Abdullah, <u>Lim Hwee San</u> and Md Noordin Abu Bakar, 2010, The Potential Application of ALOS PALSAR for Coastal Study, *Proceeding of the* **National Science Conference (NASCON 2010)**, Kota Bharu, Kelantan, Malaysia.

(13) S. M. Yusop, K. Abdullah, <u>H. S. Lim</u> and M. N. Abu Bakar, 2010, Dynamics and Circulation in the Coastal Water of Penang, Malaysia by ALOS PALSAR, *Proceeding of the* **The MRSS 6th International Remote Sensing &GIS Conference and Exhibition** *(Proceeding in CD)*, Putra World Trade Center (PWTC), Kuala Lumpur, Malaysia.

(14) S. M. Yusop, K. Abdullah, <u>H. S. Lim</u> and M. N. Abu Bakar, 2010, Observing the Effects of Atmospheric Events ove Strait of Penang, Malaysia from ALOS PALSAR, *Proceeding of the* **The MRSS 6th International Remote Sensing &GIS Conference and Exhibition** *(Proceeding in CD)*, Putra World Trade Center (PWTC), Kuala Lumpur, Malaysia.

(15) M. R. Mustapha, <u>H. S. Lim</u>, Faez M.Hassan and M. Z. Mat Jafri, 2010, Evaluation of Land Cover Features of Jeddah, Saudi Arabia Using ALOS AVNIR-2 Sensor, ***AIP Conference Proceeding: Progress of Physics Research in Malaysia: PERFIK 2009,*** Volume 1250, Digital Object Identifier:10.1063/1.3469628, p.p. 173-176.

(16) C. K. Sim, K. Abdullah, M. Z. MatJafri, and <u>H. S. Lim</u>, 2010, Assessment of ALOS PALSAR data for land cover/land use mapping in Malaysia, *Proceeding of the* **SPIE Asia-Pacific Remote Sensing Symposium,** Incheon, Korea. Multispectral, Hyperspectral, and Ultraspectral Remote Sensing Technology, Techniques, and Applications III, edited by Allen M. Larar, Hyo-Sang Chung, Makoto Suzuki, Proc. of SPIE Vol. 7857, 78571H, Digital Object Identifier: 10.1117/12.869504.